

Branching Optical Signals by Fractional Vortex Dipoles

Georgi Maleshkov^a, Peter Hansinger^b, Nikolay Dimitrov^a, Alexander Dreischuh^{a,*}, Gerhard G. Paulus^{b,c}

^a*Department of Quantum Electronics, Faculty of Physics, Sofia University, 5, J. Bourchier Blvd., Sofia-1164, Bulgaria*

^b*Institute for Optics and Quantum Electronics, Faculty of Physics and Astronomy, Friedrich-Schiller-University, Max-Wien-Platz 1, D-07743 Jena, Germany*

^c*Helmholtz-Institute Jena, Helmholtzweg 4, D-07743 Jena, Germany*

Abstract

We study the evolution and interaction of semi-infinite dark beams carrying phase dislocations, where step- and screw-like phase profiles are combined. Similar to dark beams with a finite length, semi-infinite dark beams tend to move in transversal direction with respect to their background beam. In addition, they develop a snake-like instability and optical vortices detach from their bending ends. We are looking for appropriate conditions to control the process of concatenating and crossing the ends of several such semi-infinite dark beams in a way suitable for probe-beam branching and routing in self-defocusing Kerr nonlinear media. Collinear and perpendicular probe beam propagation in the optically-induced guiding structures is modeled and analyzed with respect to the branching efficiency to respective virtual output channels.

Keywords: Kerr nonlinearity, self-defocusing, phase dislocation, dark beam, fractional vortex dipole, all-optical interaction, all-optical guiding

PACS: 42.65.Tg, 42.65.Wi, 42.65.Jx, 42.65.Hw

1. Introduction

The propagation of optical beams in nonlinear media (NLM) has been a subject of continued interest for more than four decades due to the possibility of creating reconfigurable waveguides through an intensity-dependent

*Corresponding author. Tel.: (+359 2) 8161 611; fax: (+359 2) 868 89 13.

Email address: ald@phys.uni-sofia.bg (Alexander Dreischuh)

refractive index change [1, 2]. Such optically-induced waveguides can guide weak signal beams and pulses [3, 4]. This motivates the investigation of novel techniques for manipulating the transverse beam dynamics and opens possibilities for the realization of waveguides with complex geometries. Besides their intriguing physics, the particular interest in dark spatial solitons (DSSs) is motivated by their ability to induce gradient optical waveguides in bulk self-defocusing NLM [1, 4, 5, 6, 7, 8].

The only known truly two-dimensional (2D) DSSs are optical vortex solitons [5] whereas in one transverse spatial dimension the DSSs manifest themselves as dark stripes [9]. Generating the fundamental 1D DSS requires a phase profile with odd parity as an initial condition. This corresponds to a π -phase jump centered along the irradiance minimum of the stripe (i.e. to a step-like phase dislocation). Optical vortex solitons, in contrast, have a helical (screw-type) phase profile described by an $\exp(im\varphi)$ phase factor, where φ is the azimuthal coordinate and the integer number m is the so-called topological charge. 1D and 2D fundamental DSSs of these types have the common feature of zero transverse velocity with respect to the background beam if no perturbations are present. A variable number of quasi-2D dark spatial solitons of adjustable transverse velocities can be generated [10] either by a proper choice of the initial phase profile (odd or even parity), or the width of the crossed 1D dark beams, or the background-beam intensity.

On the other hand the field of singular optics also knows dark (or grey) waves that slowly change their parameters even when they are generated from perfectly odd initial conditions. A classical example is the ring dark solitary wave [11, 12, 13, 14]. In their pioneering analysis [15], Nye and Berry conjectured that phase dislocations with a combination of a step- and screw-like phase profile (fractional vortex dipoles, FVDs) cannot exist. Nonetheless, indications for their existence were found [16, 17] for two interacting optical vortices of opposite topological charges. Moderate saturation of the medium's third-order nonlinearity enabled the suppression of the snake instability of crossed 1D dark solitons and the identification of 1D odd dark beams of finite length containing mixed-type (step-screw or edge-screw) phase dislocations [18, 19]. Later on, such odd dark beams with step-screw phase dislocations were experimentally generated under controllable initial conditions by computer-generated holograms [20]. The data confirmed [20] that one can effectively control the steering dynamics of such beams by varying the magnitude and/or the length of the 1D part of the phase jump. Although two different schemes for directional coupling of signal beams by steering FVD

beams were proposed in Kerr media with negative nonlinearities [21], the first successful experiment was conducted only recently in biased photorefractive medium with a positive nonlinearity [22].

In this work we numerically analyze two different nontrivial interaction schemes between ordered semi-infinite FVDs in a local self-defocusing NLM and model the branching and routing of probe beams inside the optically-induced reconfigurable interconnects. The first interaction scenario modeled is collinear - i.e. both the dark (pump) and the bright (probe) beam propagate in parallel through the NLM. In the second scenario the probe beams propagate perpendicular to the propagation direction of the dark beams, i.e. parallel to the dark beams themselves. Within a certain distance along the NLM, the inherently restless semi-infinite FVDs concatenate to form structures resembling cross-connects. The ability of these cross-connects to guide and redirect probe beams propagating perpendicularly are numerically investigated.

2. Numerical procedure

The mixed edge-screw phase dislocation of the FVD consists of an one-dimensional phase step of length $2b$, which ends, by necessity, with pairs of phase semi-spirals with opposite helicities. The phase profile of this mixed-phase dislocation can be described by

$$\Phi^{ES}(x, y) = \frac{\Delta\Phi}{2\pi} \left[\arctan\left(\frac{y}{x+b}\right) - \arctan\left(\frac{y}{x-b}\right) \right], \quad (1)$$

where $\Delta\Phi$ stands for the magnitude of the step portion of the dislocation and x and y denote the transverse Cartesian coordinates parallel and perpendicular to the dislocation. An increase in the odd dark beam's transverse velocity can be achieved [20] by decreasing $\Delta\Phi$. Here, however, we refrain from exploiting this in order to keep the dark beam contrast and the refractive index modulation as high as possible. All the data in this work refer to $\Delta\Phi = \pi$. A surface plot of the edge-screw phase dislocation is shown in Fig. 1. The slowly-varying electric field amplitude of a single FVD with such mixed edge-screw phase dislocation is assumed to be *tanh*-shaped and, when centered on the background beam, of the form

$$E^{ES}(x, y, z = 0) = \sqrt{I_0} B(x, y) \tanh[r_{\alpha,\beta}(x, y)/a] \exp[i\Phi^{ES}(x, y)]. \quad (2)$$

Here

$$r_{\alpha,\beta}(x, y) = [\alpha(x + \beta b)^2 + y^2]^{1/2} \quad (3)$$

is the effective radial coordinate and the parameters α and β are defined as follows

$$\alpha = \begin{cases} 0 & \text{if } |x| \leq b \\ 1 & \text{and } \beta = -1 \text{ for } x > b. \\ 1 & \text{and } \beta = 1 \text{ for } x \leq -b \end{cases} \quad (4)$$

In order to avoid any influence of the finite background beam of super-Gaussian form

$$B(x, y) = \exp\{-(x^2 + y^2)/w^2\}^8, \quad (5)$$

its width w is chosen to exceed the initial dark beam width a by a factor of more than 20.

The numerical simulations of the FVD propagation along the local Kerr NLM are carried out using the (2+1)-dimensional nonlinear Schrödinger equation

$$i\partial E/\partial(z/L_{Diff}) + (1/2)\Delta_T E - \gamma|E|^2 = 0, \quad (6)$$

which accounts for the evolution of the slowly-varying optical beam envelope amplitude E under the combined action of local nonlinearity and diffraction. Here Δ_T is the transverse part of the Laplace operator and $\gamma = L_{Diff}/L_{NL}$, where $L_{Diff} = ka^2$ and $L_{NL} = 1/(k|n_2|I)$ stand for the diffraction and nonlinear length of the dark beam respectively. The minus sign in Eq. 6 means that a self-defocusing nonlinearity is used, which is a necessary conditions for dark spatial soliton formation and for waveguiding by dark beams. In the above notations, k is the wave number inside the medium and I is the peak field intensity. The transverse spatial coordinates (x and y) are normalized to the odd dark beam width a . Equation 6 was solved numerically by means of the split-step Fourier method with a computational window spanning over 1024×1024 grid points. As a standard test we modeled the formation of a fundamental 1D dark spatial soliton and compared it to the diffraction-compensated dark beam formed by a quasi-infinite FVD (dipole much longer than the background beam; $2b \gg w$) (Fig. 2, open circles and solid curve, respectively). The figure shows that the vanishing transverse velocity of this self-sustained FVD dark beam makes it indistinguishable from an 1D dark spatial soliton. For comparison, the dashed curve in Fig. 2 shows the input FVD beam diffracted at a distance $z = 6L_{Diff}$, i.e. in the absence of a nonlinear medium. Unless stated otherwise, the background beam intensity in

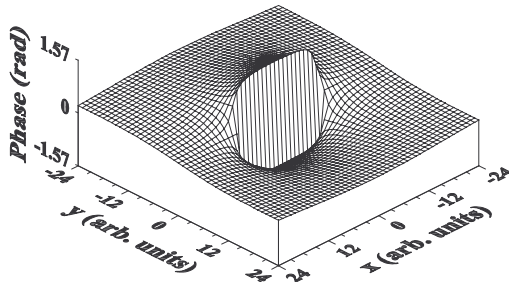


Figure 1: Edge-screw mixed phase dislocation (fractional vortex dipole, FVD) described by Eq. 1.

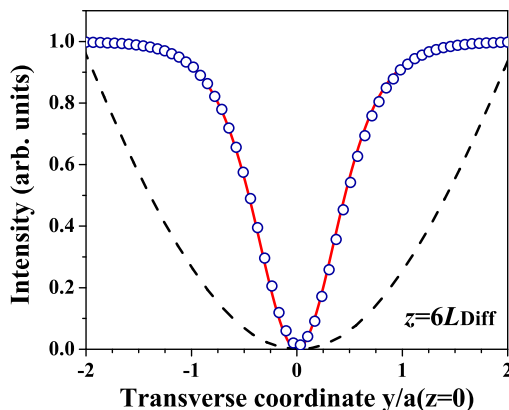


Figure 2: Cross-sections of the input quasi-infinite FVD (solid red curve) and of the fundamental 1D DSS at $z/L_{NL} = 6$ (open circles). Dashed curve – FVD diffracted at the same distance.

the following simulations is kept equal to that needed to form a fundamental 1D DSS of infinite length ($I = I_{SOL}^{1D}$, i.e. $\gamma = 1$).

3. Evolution of the fractional vortex dipoles

As shown in previous analyses of odd dark beams with mixed step-screw dislocations [20, 21], the background-beam intensity has a weak influence on the dark beam's steering. Negative nonlinearity however is important for keeping the optically induced refractive index modulation (e.g. dark beam profile and refractive index profile) steep, which is crucial for all-optical guiding, deflection, and switching of signal beams or pulses. Generally, odd dark beams of finite-length and mixed phase dislocations become shorter and flatter during their propagation in nonlinear media. This causes a power density

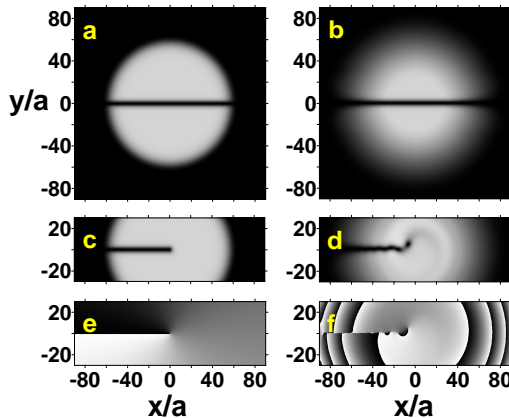


Figure 3: Upper row - Power density distributions of an infinite FVD beam at the entrance of the NLM (a) and at a nonlinear propagation distance $z/L_{NL} = 6$ (b). Middle and bottom rows - Power density (c,d) and phase distributions (e,f) of a semi-infinite FVD beam at the same distances. $I = I_{SOL}^{1D}$. The lower four images are truncated to show the significant parts of the computational windows only. An animation of the FVD beam propagation can be found here.

redistribution on the background beam that creates peaks behind the odd dark beams. The self-defocusing nonlinearity tends to suppress the peak's growth and contributes (along with diffraction) to their broadening [23]. When the length $2b$ of the FVD beam is much larger than the background beam diameter (and the computational window) and one end of the FVD is centered on the background beam, we will denote this FVD beam as "semi-infinite". In the upper row in Fig. 3 we show the power density distribution of a quasi-infinite FVD beam at the entrance of the NLM (Fig. 3a) and at $z/L_{NL} = 6$ (Fig. 3b) for $I = I_{SOL}^{1D}$. Fig. 3b is identical to that of the one-dimensional fundamental DSS (see also Fig. 2). In the second row we show the input (Fig. 3c) and output power density distribution (Fig. 3d) of a semi-infinite FVD at the same nonlinear propagation distance. It can be seen that the semi-infinite FVD beam develops a snake-like instability [24] and that a vortex detaches from the rest of the dark beam. Closer inspection of the respective phase profile (Fig. 3f) shows that four vortices with alternating topological charges are formed, three of them with highly overlapping cores. As a next step let us consider the structure and evolution of two semi-infinite FVDs oriented in opposite directions (see Fig. 4). In order to get a higher modulation depth in the interaction region near the center of the background, we shifted the ends of the FVD beams out of the center, which

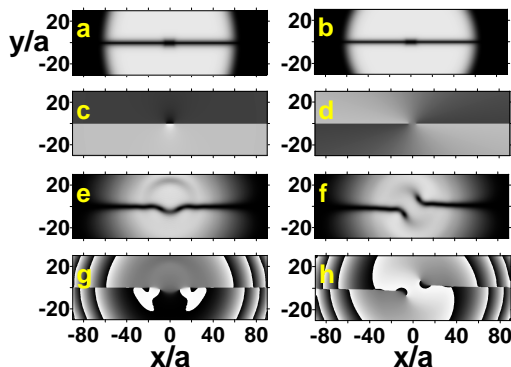


Figure 4: Power density (odd rows) and phase distributions (even rows) of pairs of overlapping ($\Delta = 2.6a$) inline semi-infinite FVD beams in the case of *opposite* (left column) and *equal* helicities (right column) of the phase semi-spirals. Top two rows - $z = 0$, bottom two rows - at the exit of the NLM ($z/L_{Diff} = 6$). $I = I_{SOL}^{1D}$.

results in an overlap of the two FVDs of $\Delta = 2.6a$. The two characteristic cases – opposite (left column) and equal phase helicities (right)– are shown in Fig. 4. In both cases the overlapping of the FVD beams causes a larger modulation in the center as compared to the remaining part of the composite dark beam. This excess ”lack of energy” is emitted as dispersive waves perpendicular to the FVD beams. In the case of opposite helicities (Fig. 4, left column), the phase distribution in the overlapping region resembles a mixed phase dislocation of limited length and the FVDs move in transverse direction, which is characteristic for beams with such dislocations. In the present situation the signature of this effect is the bending of the dark stripe. In the second case, i.e. FVDs with opposite helicities (Fig. 4b,d), the ends of the semi-infinite beams move in opposite directions and evolve almost like independent semi-infinite FVD (see frames d) and f) in Fig. 3).

For the further discussion, let us concentrate on the following three possible cases:

Case A: Pair of two parallel one-dimensional dark beams with pure one-dimensional phase dislocations of magnitude π . For consistency, the larger dark beam width in their central parts is identical to cases B) and C) where it is a result of an intentional overlapping of the FVD beams.

Case B: Pair of two inline semi-infinite FVD beams for which the overlapping FVDs have *opposite* helicities, whereas the two pairs have *opposite* phase distributions.

Case C: Pair of two inline FVD beams for which the overlapping semi-

infinite FVDs have *equal* helicities, whereas the two pairs of semi-infinite FVDs have phase distributions with the *same* gradients.

In all three cases the distance over which the FVD beams overlap is $\Delta = \pm 1.3a$ and the vertical offset from the background beam diameter is $\Delta y = \pm 1.8a$. Although the amplitude distributions in all three cases are identical (Fig. 5, second row), the entirely different phase profiles (Fig. 5, first row) govern distinctive transverse dynamics along the NLM. It is worth mentioning that when two *identical* semi-infinite FVDs are aligned on a line, the neighboring phase semi-spirals have *opposite* helicities, no matter if the FVDs overlap or not. The phase profile of a single FVD beam of limited length ends also by semi-spirals with opposite helicities (see Fig. 1). Since the steering direction is phase-dependent [20, 21] the FVD beam overlapping does not alter it.

In Case A we simply have propagation and interaction (weak repulsion in a local NLM [25, 26]) of closely-spaced one-dimensional dark spatial solitons. The modulation in the middle of these beams leads to an emission of a dispersive wave causing a perturbation (Fig. 5, left column, $z = 3L_{NL}$). As a result, the dark beams slightly bend but do not develop a snake instability and also do not decay into pairs of vortices (up to $z = 6L_{NL}$) (Fig. 5, left column). For probe signals entering the NLM both collinearly and perpendicularly to the background beam, the optically-induced waveguiding structure in this case consists essentially of two parallel planar waveguides.

In Case B, due to the specific orientation of the phase profiles of the FVD beams, the central parts of the dark beams bend inwards and overlap, thus forming a cross-like structure at $z = 3L_{NL}$. When the nonlinear propagation path length is increased up to $z = 6L_{NL}$, the beams in this region repel each other, bend, split, and decay into four (still highly overlapping) optical vortices. Hence, the proper position for the probe beam to enter the NLM at right angles is at $z = 3L_{NL}$. The effective waveguide structure for the probe beam in this case is a symmetric X-junction (input inline with one of the outputs). In the collinear configuration the situation will be qualitatively the same.

The effective waveguiding structure for perpendicularly propagating probe beams that develops Case C resembles bent planar waveguides. If the probe beam enters the NLM at $z = 1L_{NL}$, it will see the upper left planar waveguide merging into the lower right waveguide. At smaller and longer propagation distances for the pump the connection between the FVDs (and the effective waveguide) is broken. Qualitatively, the four FVD beams evolve more or

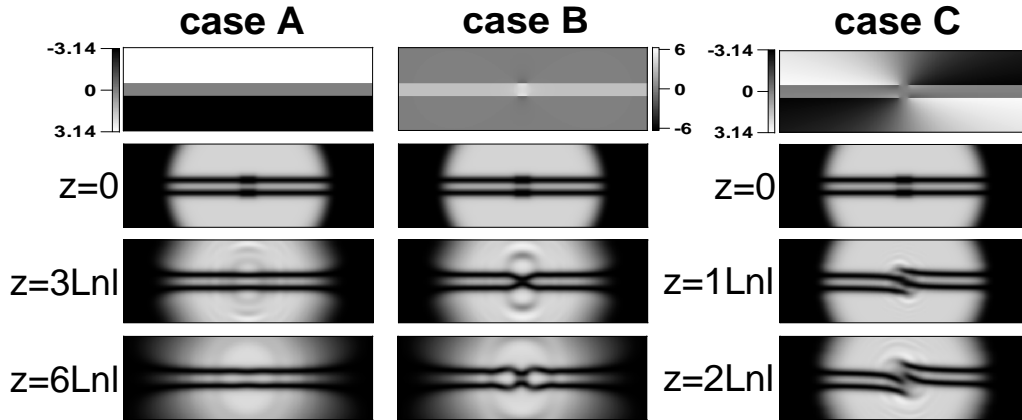


Figure 5: Phase profiles (upper row) and power density distributions of pairs of inline semi-infinite and overlapping FVDs at the entrance of the NLM and at distances $z = 3L_{NL}$ and $6L_{NL}$ for case A and case B and at $z = 1L_{NL}$ and $2L_{NL}$ for case C. Hyperlinks-respective avi-movies.

less independently for Case C. Of course, because of the inherent dynamics of the FVD beams, the probe beam guiding efficiencies can not be expected to be 100%. In cases B and C therefore one can expect certain (different) branching ratios for the incoming signal beams. Moreover, in the transverse pump-probe geometry the effective nonlinear interaction length extends over the pump beam cross section only.

4. Branching of probe beams inside the optically-induced guiding structures

The incoming probe beams are modeled to be Gaussian with widths equal to the vertical extent of the one-dimensional dark soliton shown in Figs. 2 and 3. The NLM can be visualized as a cuboid (see Fig. 6). Its depth (along the z -axis) extends up to $6L_{NL}$ in the cases A and B, and up to $2L_{NL}$ in case C. In the collinear propagation regime, both dark FVD beams and bright probe beams propagate along the z -axis. The probe beam evolution is modeled separately from the pump beam propagation by solving the (linear) slowly-varying envelope equation for the probe beam amplitude S

$$i\partial S/\partial z + [1/(2L_{DS})](\partial^2/\partial x^2 + \partial^2/\partial y^2)S - |E|^2 S/L_{NL} = 0. \quad (7)$$

When the probe beam enters the NLM perpendicularly at $z = 3L_{NL}$ (cases A and B) or at $z = L_{NL}$ (case C) it evolves along the propagation coordinate

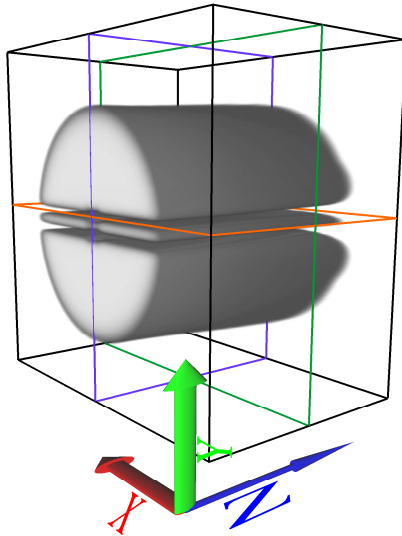


Figure 6: Schematic view of the background beam carrying the FVD beams inside the non-linear medium with the used notation of the coordinate system axes. Collinear propagation is along the z -axis, perpendicular propagation – along the x -axis. The thin horizontal and vertical (color) lines cross approximately at the positions where the probe beams enter the NLM.

x diffracting and experiencing the refractive index modulation mainly in the (y, z) plane due to the background beam with the embedded FVDs (see Fig. 6). This is modeled separately, by solving the equation

$$i\partial S/\partial x + [1/(2L_{DS})](\partial^2/\partial y^2 + \partial^2/\partial z^2)S - |E|^2 S/L_{NL} = 0. \quad (8)$$

Here $L_{DS} = k_S a_S^2$ is the diffraction length of the bright probe beam of width a_S such that $L_{DS} = L_{Diff} = L_{NL}$. The computational grid for the probe beams spans over 256×256 grid points in order to use the stored 256 distributions for the pump electric-field amplitude and to follow the evolution of the probe wave. Each probe beam enters the induced waveguides exactly in the center (at $z = 1L_{NL}$ for case C, and at $z = 3L_{NL}$ for cases A and B). In Fig. 6 we show a schematic view of the NLM with the used notation of the coordinate system axes. The blue (green) line cross the red line approximately at the position where the collinear (perpendicular) probe beam enters the NLM. In addition, the intensity distribution of the background beam is shown for Case A.

4.1. Collinear probe beam propagation

The obtained numerical results are summarized in Fig. 7 and in Table 1. For better visibility, in each frame in Fig. 7 only some 8% of the total computational area is shown. In this case the input probe beams (IN) enter the NLM centered in the respective dark-beam-induced waveguides as marked in Fig. 6. The parallel pump and probe beam propagation is along the z -axis. The power density profiles of the probe beams at the exit of the NLM ($z = 6L_{Diff}$ for cases A and B; $z = 2L_{Diff}$ for case C) are labelled accordingly. The horizontal probe beam spreading in case A is indicative for the probe beam diffraction at $z = 6L_{Diff}$. The horizontal dashed (yellow) line denotes the (x, z) symmetry plane separating the two imaginary output channels in cases A and B. In case C the parallel solid lines denote the three virtual output channels for which the probe-beam branching efficiencies are shown in Table 1. In cases A and B where two virtual output channels are considered, the guiding efficiency in the middle one (M) is marked as "not related" (n.r.). The 100%-mark in column IN in Tables 1 and 2 denotes which probe beam is launched in the respective input channel. The accuracy in estimating the efficiencies is 2%. The first three rows (upper- U , middle- M , and lower- L) refer to the probe beam entering the upper guiding structure (with 99% efficiency), the lower three rows – to probe beam entering the lower dark structure. Generally, the dark guiding structures evolve symmetrically with respect to the (x, z) -plane and the probe beam branching ratios should be the same (but inverted) for both probe beams. The small asymmetry (70%/30% vs. 65%/35%) is a result of an intentional shift of the border between the two imaginary output channels in case A and B to locate it at the maximal modulation depth of the branched signal. In case C the different branching ratios for the signal beams entering the upper and lower guiding structure result from the lack of symmetry of the type present in the first two cases.

4.2. Perpendicular probe beam propagation

The results for this case are shown in Fig. 8 and in Table 2. The presence of strong refractive-index gradients along the y -axis for $I = I_{SOL}^D$ improves the linearly redistributed signal (see Fig. 8, column L) to channels 1 and 2 from 44%/20% to 72%/18% when channel 1 is initially addressed (see Table 2). When the probe beams is entering initially channel 2, the (inverted) proportionality is quite similar. By changing the phase profiles of the pairs of overlapping pump FVD beams the cited 72% guiding efficiency when input channel 1 is addressed, can be changed to 66% (case B) and to 61% (case

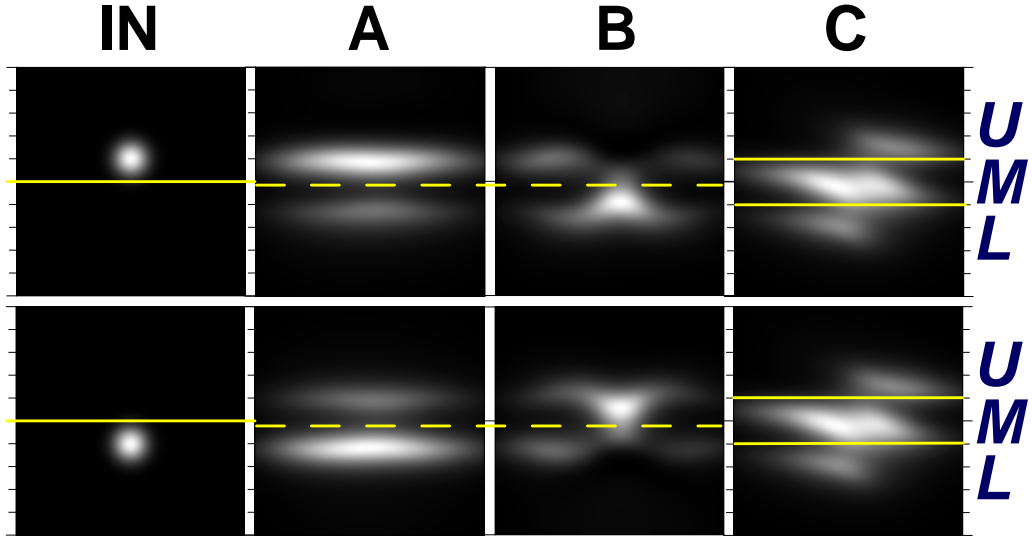


Figure 7: **Collinear propagation:** Input probe beams (IN) entering the NLM being centered in both dark beam-induced waveguides as marked in Fig. 6 and propagating along the z -axis parallel to the pump. The power density profiles of the probe beams at the exit of the NLM in the nonlinear regimes ($\gamma = 1$) for cases A, B, and C are correspondingly denoted. The horizontal dashed (yellow) line indicates the (x, z) symmetry plane separating the two imaginary output channels in cases A and B. The parallel solid lines in case C separate the virtual three output channels for which the probe-beam branching efficiencies are also summarized in Table 1.

C). The behavior is qualitatively the same when input channel 2 is initially addressed. The second part of Table 2 refers to a separate set of simulations for $I = 2I_{SO}^{1D}$. In this way the branching ratios can be changed from e.g. 72%/18% to 82%/14% in case A and from 66%/25% to 69%/21% in case B when initially channel 1 is addressed only. As seen from Table 2, the general tendency in cases A and B is that the increase of the background-beam intensity leads to a deeper modulation of the refractive index in the straight parts of the waveguides and to a somewhat weaker probe beam branching in the interaction region. In case C, one optically-induced waveguide becomes coupled to another one whereas the other two become decoupled only (Fig. 5, right column, $z = L_{Diff}$), so the higher intensity leads to a weak increase of the coupling efficiency into one of the channels and to a decrease of this efficiency into the other channel.

Table 1: **Collinear propagation:** Probe beam branching efficiencies in two (cases A, B; $z = 6L_{Diff}$) and in three output ports (case C; $z = 2L_{Diff}$), respectively, for $\gamma = I/I_{SO}^{1D} = 1$. (IN)-input; (n.r.)-not related.

Channel	IN	A	B	C
U	99%	30%	42%	21%
M	n.r.	n.r.	n.r.	52%
L	1%	70%	57%	26%
U	1%	65%	54%	16%
M	n.r.	n.r.	n.r.	47%
L	99%	35%	45%	36%

Table 2: **Perpendicular pump and probe beams:** Probe beam branching efficiencies in the different propagation regimes; (L)-linear; (A), (B), and (C) - nonlinear propagation regimes for cases A, B, and C, respectively, for $\gamma = I/I_{SO}^{1D} = 1$ and $\gamma = 2$. (IN)-input.

	Channel	IN	L	A	B	C
$\gamma = 1$	1	100%	44%	72%	66%	61%
	2	0%	20%	18%	25%	25%
	1	0%	20%	19%	24%	20%
	2	100%	44%	68%	63%	58%
$\gamma = 2$	1	100%	44%	82%	69%	54%
	2	0%	20%	14%	21%	26%
	1	0%	20%	14%	15%	15%
	2	100%	44%	81%	60%	60%

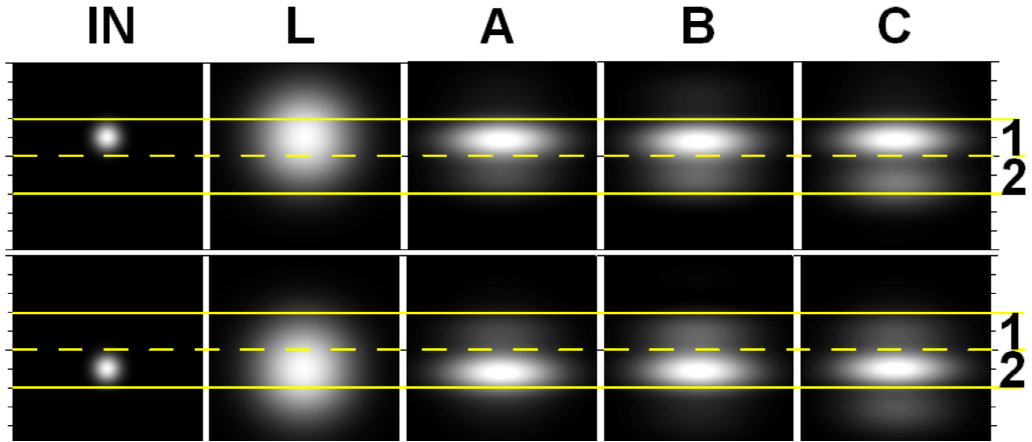


Figure 8: **Perpendicular pump and probe beams:** Input probe beams (IN) entering the NLM perpendicularly to the pump, in the center of the imaginary cell containing the NLM (Fig. 6) and propagating along the x -axis. (L): Output power density distributions of the probe beams propagating linearly to the exit of the cell ($x/L_{Diff}=3.5$). The results for the probe beams at the exit of the NLM in the nonlinear regimes for cases A, B, and C are correspondingly denoted. $\gamma = 1$. The horizontal dashed (yellow) line indicates the (x, z) input symmetry plane, whereas the solid lines denote the virtual output channels for which the probe-beam branching efficiencies are summarized in Table 2.

5. Conclusion

The existence and evolution of ordered structures of odd dark beams of semi-infinite length carrying edge-screw phase dislocations (fractional vortex dipoles) were studied in a local self-defocusing Kerr nonlinear medium. We found appropriate conditions for controlling the process of crossing dark beams in a way suitable for probe-beam cross-switching. The proposed technique strongly relies on the features of these beams that a quasi-infinite vortex dipole (dipole much longer than the background beam) evolves into an one-dimensional dark spatial soliton and that a single semi-infinite fractional dipole bends and develops a snake-like instability near the dark beam end. Depending on their phase profiles, four parallel semi-infinite fractional vortex dipoles aligned to initially form two dark stripes can evolve into two different cross-connects able to partially redirect collinearly- and perpendicularly-propagating probe optical beams at different branching efficiencies. While being still far from discussing particular practical applications, the desirable high-efficient routing of probe beams by fractional vortex dipoles seems feasible provided the interaction length in the overlapping region of the fractional

vortex dipoles and the probe beams becomes longer. The presented results provide a reasonable first step for further optimization of such schemes. The presented results provide a reasonable first step for further optimization of such schemes. Since the eventual medium nonlocality can have a substantial (not necessarily detrimental) impact [26, 27, 28, 29] on the fractional vortex dipole interaction and stability, further numerical simulations for realistic nonlinear media are under way.

6. Acknowledgments

This work was supported by the NSF-Bulgaria (grants *DO-02-0114/2008* and *DRNF-02-8/2009*), and by the DFG in the framework of Forschergruppe 532 "Nichtlineare raum-zeitliche Dynamik in dissipativen und diskreten optischen Systemen".

7. Captions for the figures

Fig.1 – Edge-screw mixed phase dislocation (fractional vortex dipole, FVD) described by Eq. 1.

Fig.2 – Cross-sections of the input quasi-infinite FVD (solid red curve) and of the fundamental 1D DSS at $z/L_{NL} = 6$ (open circles). Dashed curve – FVD diffracted at the same distance.

Fig.3 – Upper row - Power density distributions of an infinite FVD beam at the entrance of the NLM (a) and at a nonlinear propagation distance $z/L_{NL} = 6$ (b). Middle and bottom rows - Power density (c,d) and phase distributions (e,f) of a semi-infinite FVD beam at the same distances. $I = I_{SOL}^D$. The lower four images are truncated to show the significant parts of the computational windows only. An animation of the FVD beam propagation can be found here.

Fig.4 – Power density (odd rows) and phase distributions (even rows) of pairs of overlapping ($\Delta = 2.6a$) inline semi-infinite FVD beams in the case of *opposite* (left column) and *equal* helicities (right column) of the phase semi-spirals. Top two rows $z = 0$, bottom two rows - at the exit of the NLM ($z/L_{Diff} = 6$). $I = I_{SOL}^D$.

Fig.5 – Phase profiles (upper row) and power density distributions of pairs of inline semi-infinite and overlapping FVDs at the entrance of the NLM and at distances $z = 3L_{NL}$ and $6L_{NL}$ for case A and case B and at $z = 1L_{NL}$ and $2L_{NL}$ for case C. Hyperlinks-respective avi-movies.

Fig.6 – Schematic view of the background beam carrying the FVD beams inside the nonlinear medium with the used notation of the coordinate system axes. Collinear propagation is along the z -axis, perpendicular propagation - along the x -axis. The horizontal and vertical tiny (color) lines cross approximately at the positions where the probe beams enter the NLM.

Fig.7 – **Collinear propagation:** Input probe beams (IN) entering the NLM being centered in both dark beam-induced waveguides as marked in Fig. 6 and propagating along the z -axis parallel to the pump. The power density profiles of the probe beams at the exit of the NLM in the nonlinear regimes ($\gamma = 1$) for cases A, B, and C are correspondingly denoted. The horizontal dashed (yellow) line indicates the (x, z) symmetry plane separating the two imaginary output channels in cases A and B. The parallel solid lines in case C separate the virtual three output channels for which the probe-beam branching efficiencies are also summarized in Table 1.

Fig.8 – **Perpendicular pump and probe beams:** Input probe beams (IN) entering the NLM perpendicularly to the pump, in the center of the imaginary cell containing the NLM (Fig. 6) and propagating along the x -axis. (L): Output power density distributions of the probe beams propagating linearly to the exit of the cell ($x/L_{Diff}=3.5$). The results for the probe beams at the exit of the NLM in the nonlinear regimes for cases A, B, and C are correspondingly denoted. $\gamma = 1$. The horizontal dashed (yellow) line indicates the (x, z) input symmetry plane, whereas the solid lines denote the virtual output channels for which the probe-beam branching efficiencies are summarized in Table 2.

8. Captions for the tables

Table 1 – **Collinear propagation:** Probe beam branching efficiencies in two (cases A, B; $z = 6L_{Diff}$) and in three output ports (case C; $z = 2L_{Diff}$), respectively, for $\gamma = I/I_{SOL}^1 = 1$. (IN)-input; (n.r.)-not related.

Table 2 – **Perpendicular pump and probe beams:** Probe beam branching efficiencies in the different propagation regimes; (L)-linear; (A), (B), and (C) - nonlinear propagation regimes for cases A, B, and C, respectively, for $\gamma = I/I_{SOL}^1 = 1$ and $\gamma = 2$. (IN)-input.

References

- [1] G. I. Stegeman, M. Segev, Science 286 (1999) 1518–1523.

- [2] Yu. S. Kivshar, B. Luther-Davies, *Phys. Rep.* 298 (1998) 81–197.
- [3] R. De La Fuente, A. Barthelemy, C. Froehly, *Opt. Lett.* 16 (1991) 793–795.
- [4] A. W. Snyder, A. P. Sheppard, *Opt. Lett.* 18 (1993) 482–484.
- [5] G. A. Swartzlander, Jr., C. T. Law, *Phys. Rev. Lett.* 69 (1992) 2503–2506.
- [6] E. A. Ostrovskaya, Yu. S. Kivshar, *Opt. Lett.* 23 (1998) 1268–1270.
- [7] A. H. Carlsson, J. N. Malmberg, D. Anderson, M. Lisak, E. A. Ostrovskaya, T. J. Alexander, Yu. S. Kivshar, *Opt. Lett.* 25 (2000) 660–662.
- [8] C. T. Law, X. Zhang, G. A. Swartzlander, Jr., *Opt. Lett.* 25 (2000) 55–57.
- [9] G. Allan, S. Skinner, D. Andersen, A. Smirl, *Opt. Lett.* 16 (1991) 156–158.
- [10] D. Neshev, A. Dreischuh, S. Dinev, L. Windholz, *J. Opt. Soc. Am. B* 14 (1997) 2869–2876.
- [11] Yu. S. Kivshar, X. Yang, *Phys. Rev. E* 50 (1994) R40–R43.
- [12] Yu. S. Kivshar, X. Yang, *Chaos, Solitons and Fractals* 4 (1994) 1745–1758.
- [13] D. Neshev, A. Dreischuh, V. Kamenov, I. Stefanov, S. Dinev, W. Fließer, L. Windholz, *Appl. Phys. B* 64 (1997) 429–433.
- [14] A. Dreischuh, D. Neshev, G. G. Paulus, F. Grasbon, H. Walther, *Phys. Rev. E* 66 (2002) 066611(1–7).
- [15] J. F. Nye, M. V. Berry, *Proc. R. Soc. London A* 336 (1974) 165–190.
- [16] V. Bazhenov, M. Soskin, M. Vasnetsov, *J. Mod. Opt.* 39 (1992) 985–990.
- [17] I. Basistiy, V. Bazhenov, M. Soskin, M. Vasnetsov, *Opt. Commun.* 103 (1993) 422–428.
- [18] A. Dreischuh, G. G. Paulus, F. Zacher, *Appl. Phys. B* 69 (1999) 107–111.
- [19] A. Dreischuh, G. G. Paulus, F. Zacher, I. Velchev, *Appl. Phys. B* 69 (1999) 113–117.
- [20] A. Dreischuh, D. Neshev, G. G. Paulus, H. Walther, *J. Opt. Soc. Am. B* 17 (2000) 2011–2016.

- [21] D. Neshev, A. Dreischuh, G. G. Paulus, H. Walther, *Appl. Phys. B* 72 (2001) 849–854.
- [22] G. Maleshkov, D. N. Neshev, A. Dreischuh, *Phys. Rev. A* 80 (2009) 053828(1–5).
- [23] G. Maleshkov, P. Hansinger, A. Dreischuh, G. G. Paulus, *Proc. SPIE* 7747 (2011) art. 77471P.
- [24] V. Tikhonenko, J. Christou, B. Luther-Davies, Yu. S. Kivshar, *Opt. Lett.* 21 (1996) 1129–1131.
- [25] K. J. Blow, N. J. Doran, *Phys. Lett. A* 107 (1885) 55–58.
- [26] A. Dreischuh, D. N. Neshev, D. E. Petersen, O. Bang, W. Krolikowski, *Phys. Rev. Lett.* 96 (2006) art. 043901.
- [27] N. I. Nikolov, D. N. Neshev, W. Krolikowski, O. Bang, J. J. Rasmussen, P. L. Christiansen, *Opt. Lett.* 29 (2004) 286–288.
- [28] D. Briedis, D. E. Petersen, D. Edmundson, W. Krolikowski, O. Bang, *Opt. Express* 13 (2005) 435–443.
- [29] Q. Kong, Q. Wang, O. Bang, W. Krolikowski, *Phys. Rev. A* 82 (2010) art. 013826.